Electronic Supplementary Material (ESI) for Nanoscale.


# Enhancing ammonium-ion storage in Mo-doped $VO_2$ (B) nanobelt-bundles anode for aqueous ammonium-ion batteries

Long Chen, Jie Zhang, Zuoshu Wang, Dewei Wang*

College of Materials Science and Engineering, North Minzu University, Yinchuan 750021, People's Republic of China.

*Corresponding author. Tel: +86 951 2067378. E-mail: wangdewei@yeah.net

**Synthesis of CuHCF**

Solution A and B were obtained by dissolving 5 mmol of $K_3[Fe(CN)_6]$ and 10 mmol of $CuSO_4$-$5H_2O$ into 50 mL of $H_2O$ solution and stirring for 15 min, then solution A and B were added dropwise into 100 mL of $H_2O$ and stirred until a green precipitate was produced, and the products were washed by centrifugation with water and ethanol, and finally, the samples were dried under vacuum at 60 °C for 24 h.

The diffusion coefficient (D) was calculated using the equation:

$$D_{ion} = \frac{4}{\pi\tau}(\frac{nV}{S})^2(\frac{\Delta E_s}{\Delta E_t})^2$$

whereas $\tau$ is the relaxation time, the $n$ is concentration and the $V$ is the molar volume, $S$ represents the contact area. The $\Delta E$s and $\Delta E$t denotes the voltage variation within a single GITT process and the voltage changes during GCD, respectively.

**Computational details**

The spin-polarized density functional theory (DFT) calculations within the generalized gradient approximation (GGA) were performed using the Vienna Ab Initio Package (VASP). The Perdew-Burke-Ernzerhof (PBE) formulation was employed for these calculations. The ionic cores were described using projected augmented wave (PAW) potentials, and the valence electrons were taken into account based on a plane wave basis set with a kinetic energy cutoff of 450 eV. To allow for partial occupancies of the Kohn−Sham orbitals, the Gaussian smearing method with a width of 0.05 eV was used. The self-consistency of the electronic energy was considered achieved when the energy change became smaller than $10^{-5}$ eV. For the optimization of equilibrium lattice constants and each ionic optimization step, a maximum Hellmann-Feynman force of 0.05 eV/Å was applied. The catalyst configurations, named $VO_2$ and Mo-doped-$VO_2$, were established and modeled as two layers in a slab configuration. A 15Å vacuum layer in the z direction separated the slab from its periodic images. A 2×2×1 Monkhorst-Pack k-point grid was utilized for Brillouin zone sampling during the structural optimization and energy calculation.

The adsorption energy (Eads) of the adsorbate molecule was determined as:

Eads = Emol/surf – Esurf - Emol

where Emol/surf represents the energy of the adsorbate molecule adsorbed on the surface, Esurf is the energy of the clean surface, and Emol is the energy of the molecule itself.

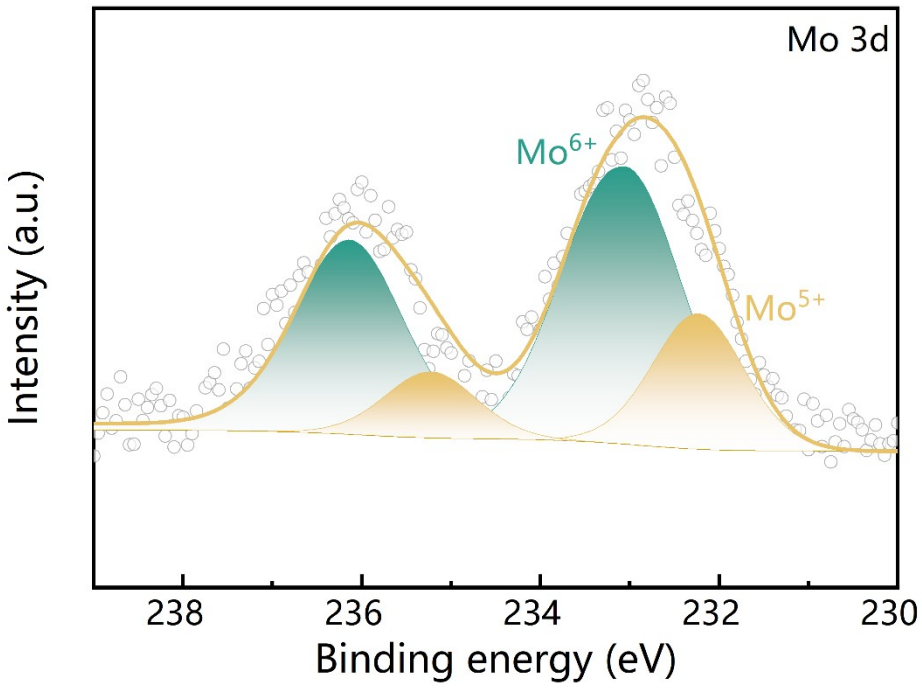


**Figure S1.** Mo 3d spectrum after argon-ion etching.

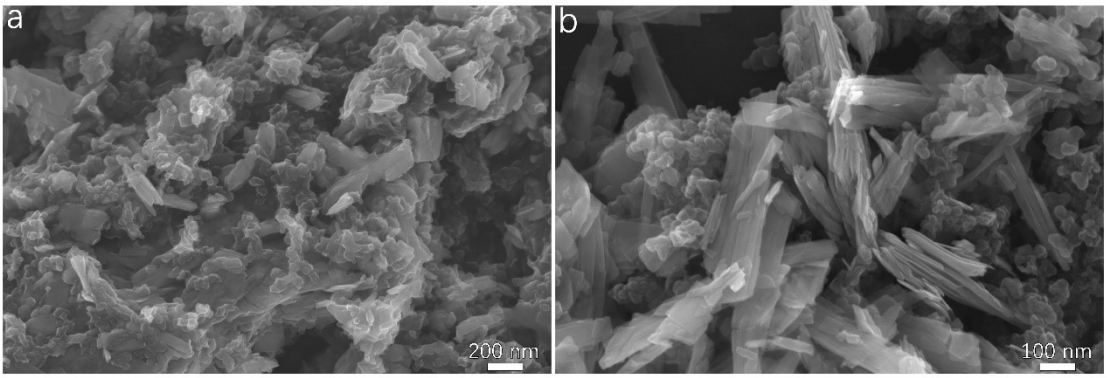


**Figure S2.** SEM images of the samples after the cycling tests, (a) PVO and (b) MVO.

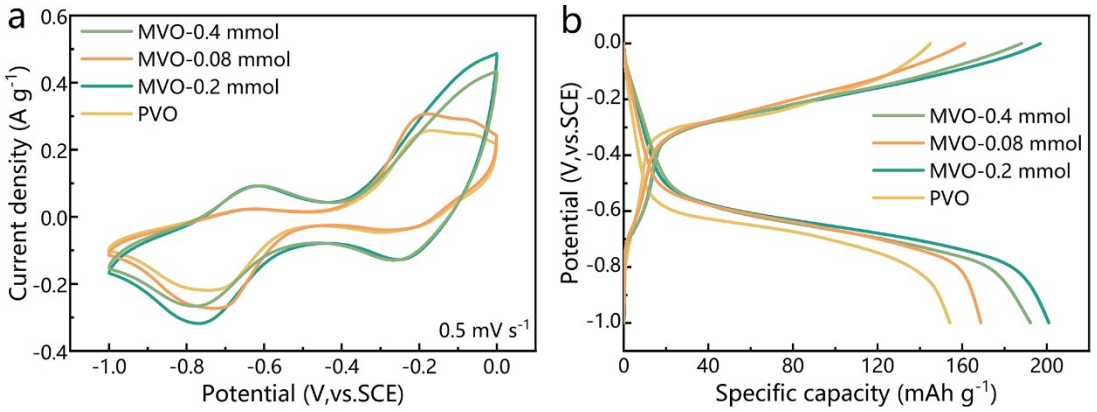


**Figure S3.** Electrochemical performance at different amounts of sodium molybdate.

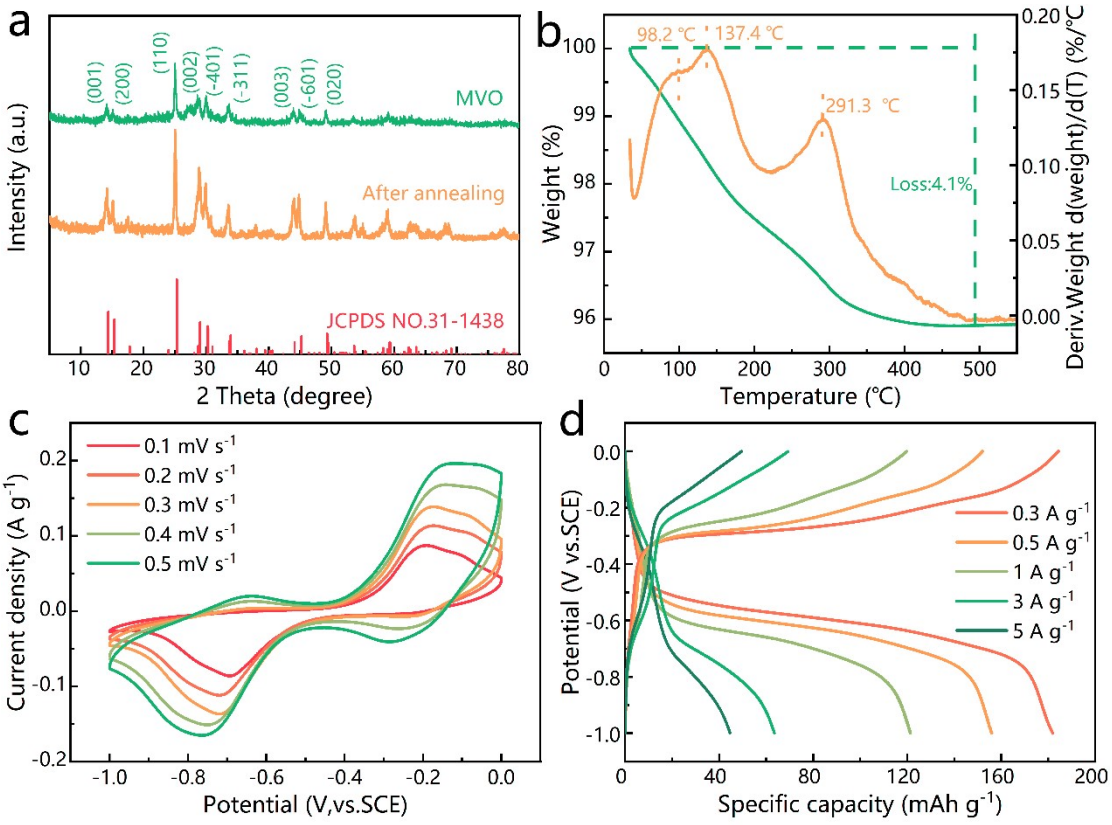


**Figure S4.** (a) XRD of MVO before and after annealing, (b) thermogravimetry analysis curves of MVO, (c) CV curves of MVO after annealing at different scanning rates, and (d) GCD curves at different current densities.

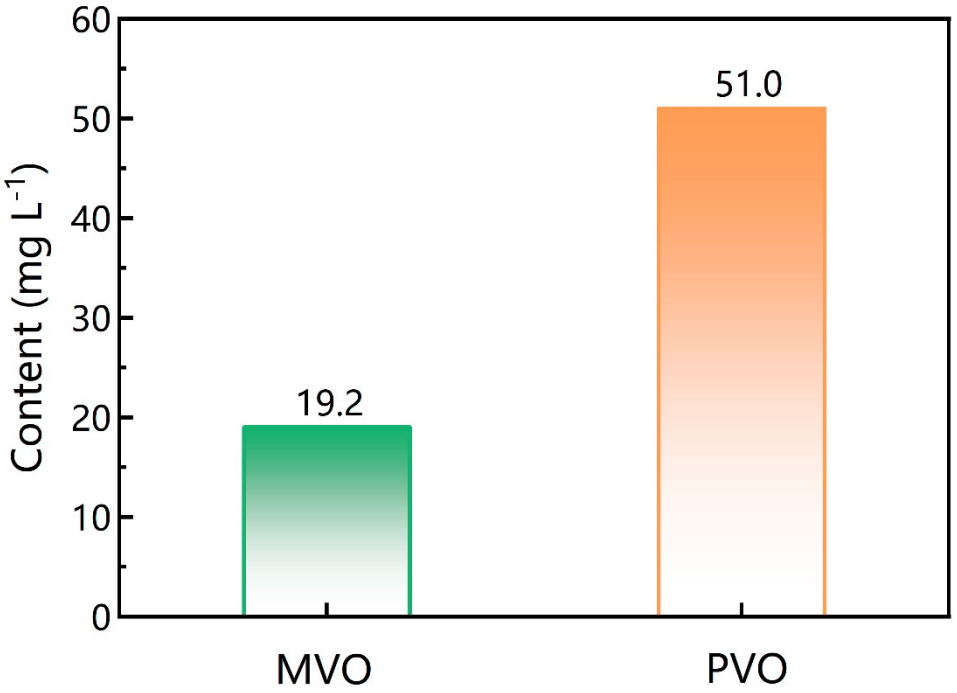


**Figure S5.** Vanadium content in electrolyte after cyclic test based on ICP-OES results.

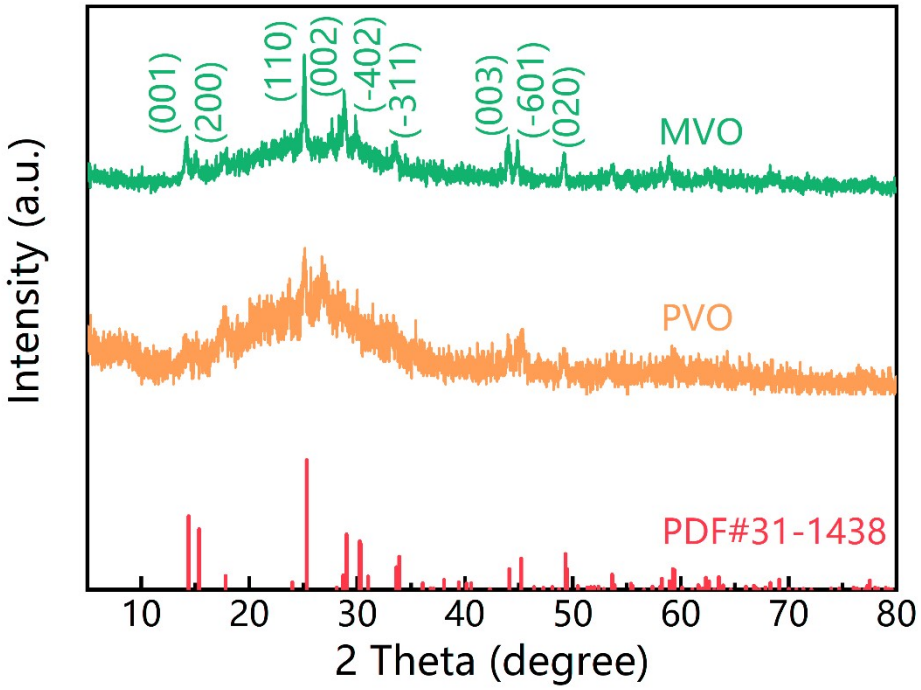


**Figure S6.** XRD patterns of the samples after the cycling tests.

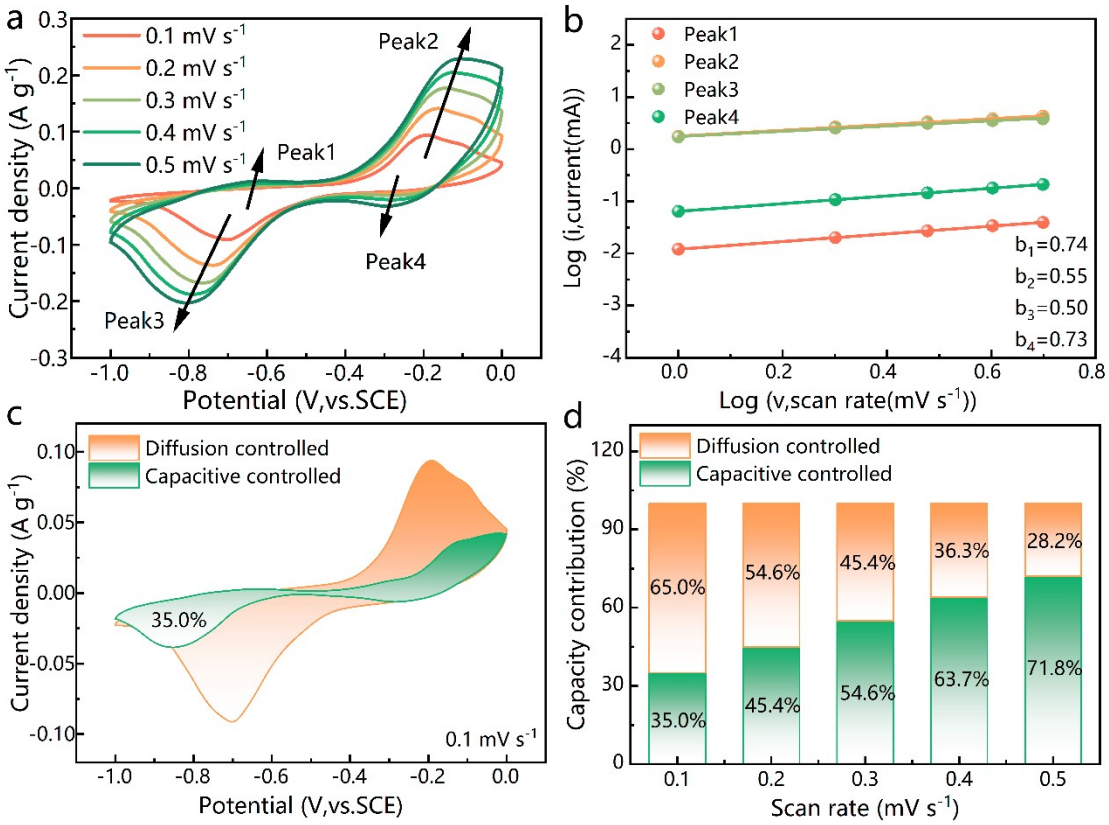


**Figure S7.** (a) CV curves of PVO at different scan rates, (b) log (peak current) versus log (scan rate) plots derived peak currents, (c) capacitive contributions at 0.1 mV $s^{-1}$, (d) diffusive and capacitive contributions at various scan rates.

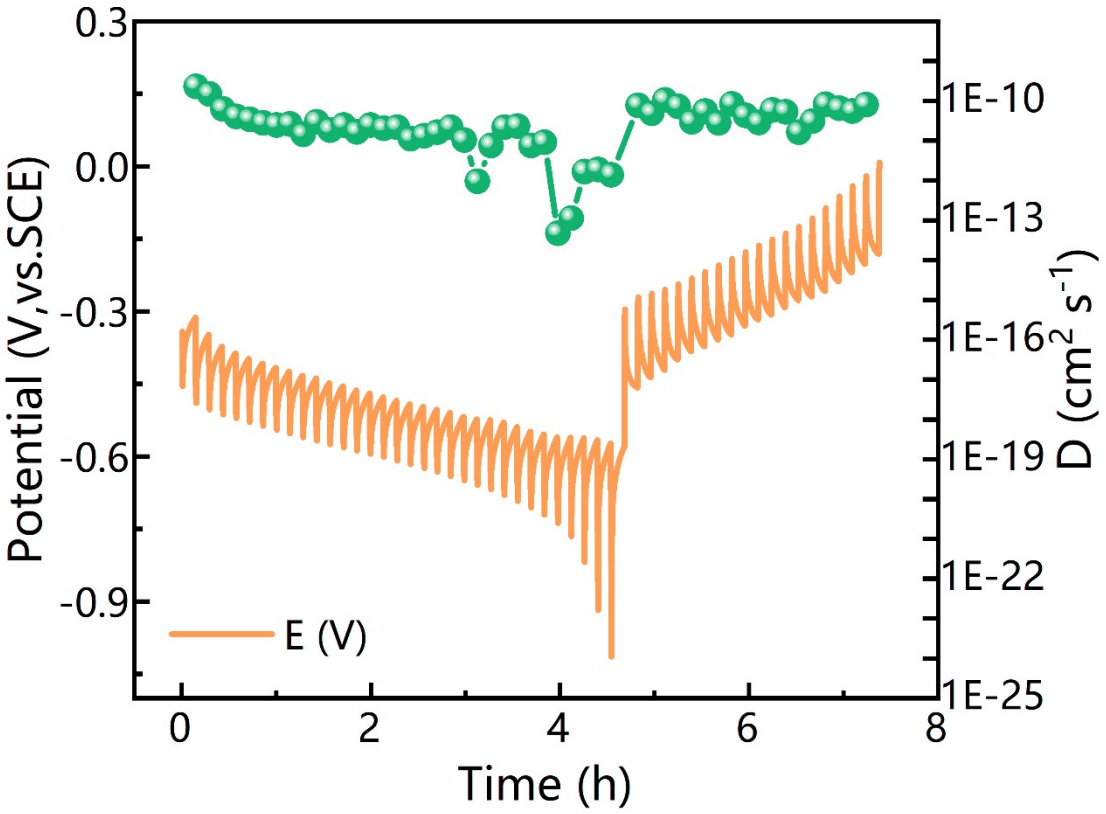


**Figure S8.** GITT curves and corresponding $NH_4^+$ diffusion coefficients for PVO.

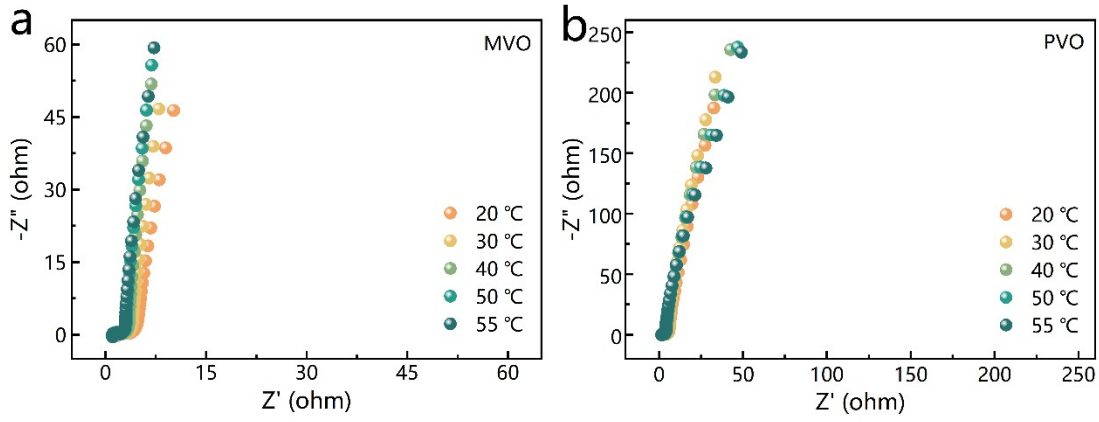


**Figure S9.** Nyquist plots of MVO and PVO at different temperatures.

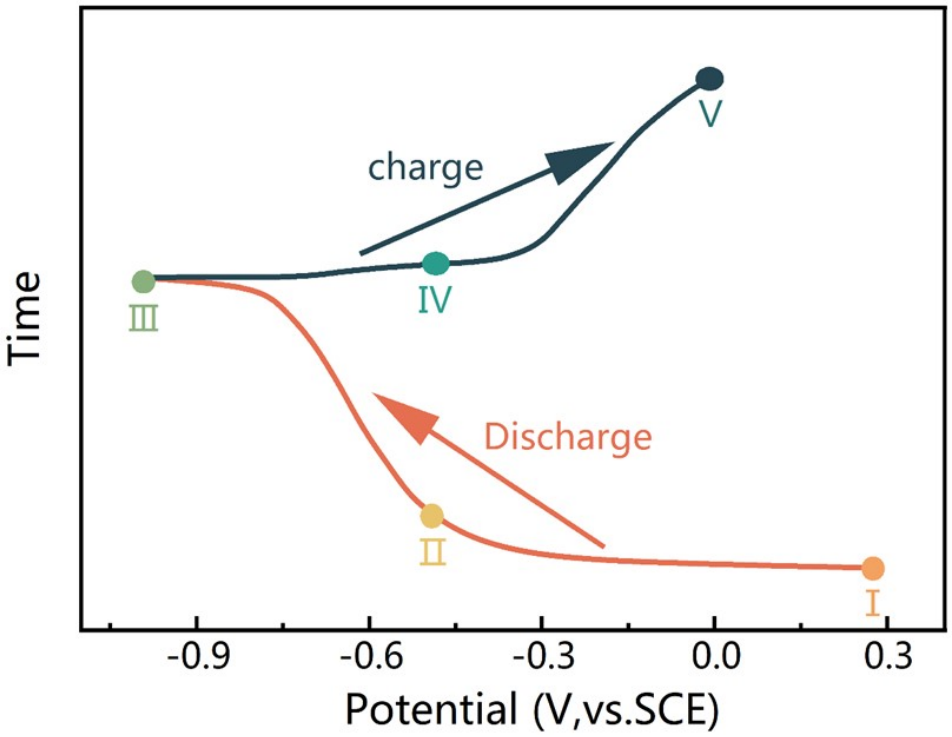


**Figure S10.** GCD profile of MVO at a current density of 0.3 A $g^{-1}$.

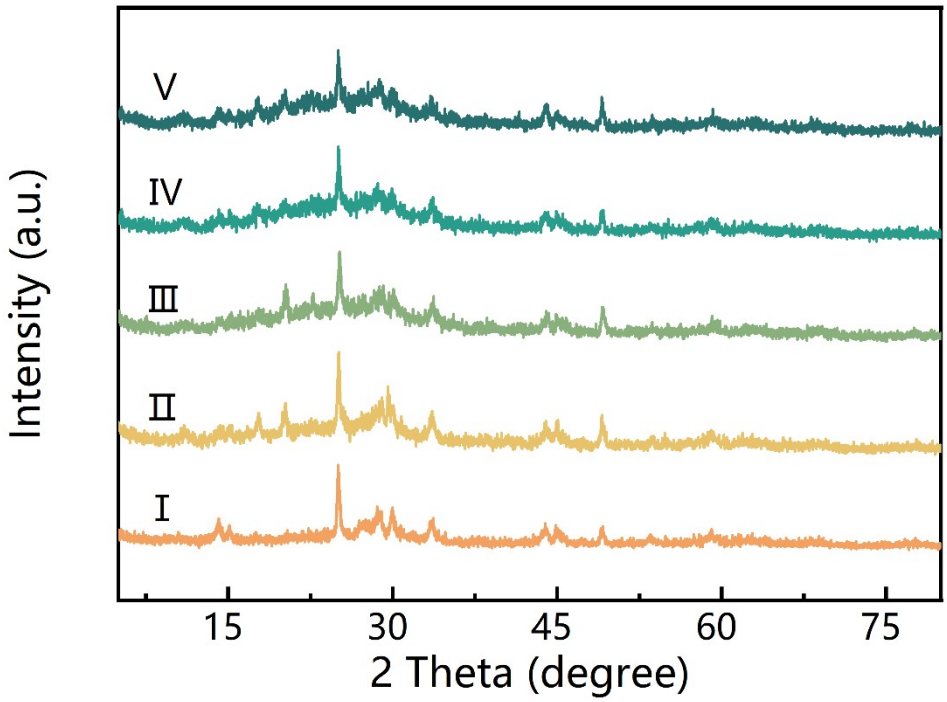


**Figure S11.** Ex situ XRD patterns at different charge-discharge states

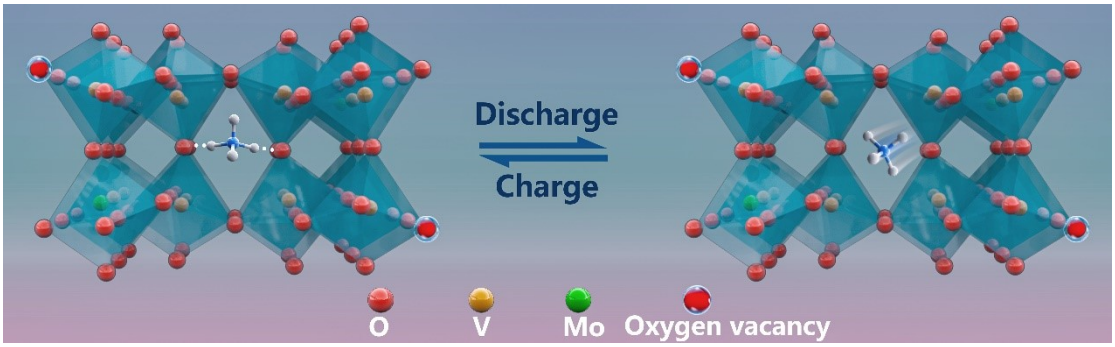


**Figure S12.** Schematic illustration of the reversible insertion and extraction process of $NH_4^+$ in MVO.

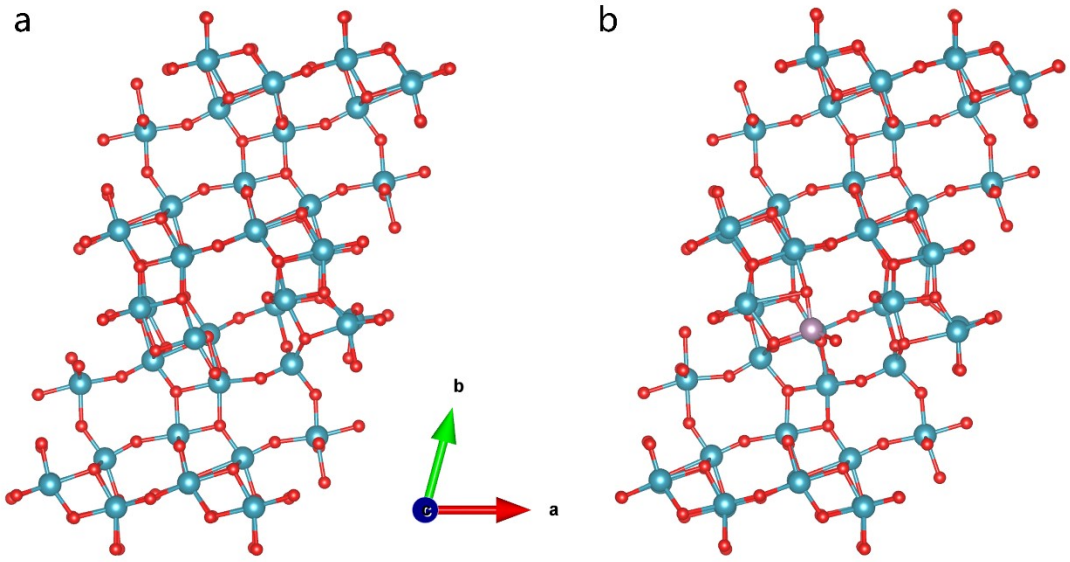


**Figure S13.** Optimized structural models of (a) PVO and (b) MVO.

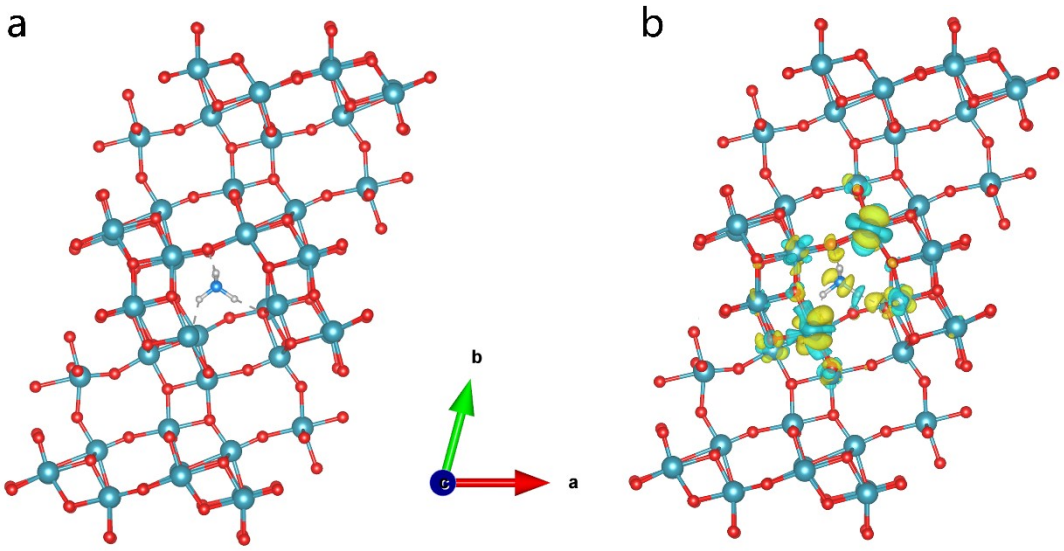


**Figure S14.** $NH_4^+$ absorption structures of (a) PVO and (b) charge density difference of PVO after $NH_4^+$ insertion.

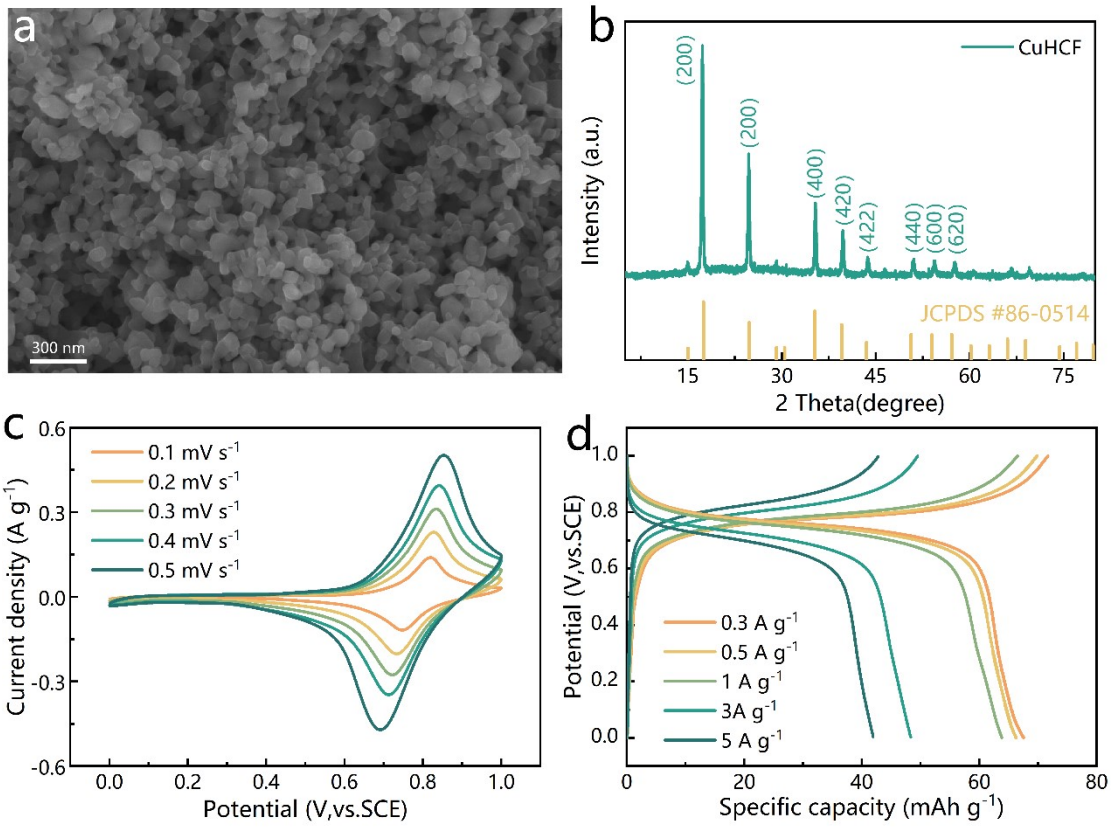


**Figure S15.** Morphology and electrochemical performance of CuHCF electrode, (a) SEM image, (b) XRD pattern, (c) CV, and (d) GCD curves.

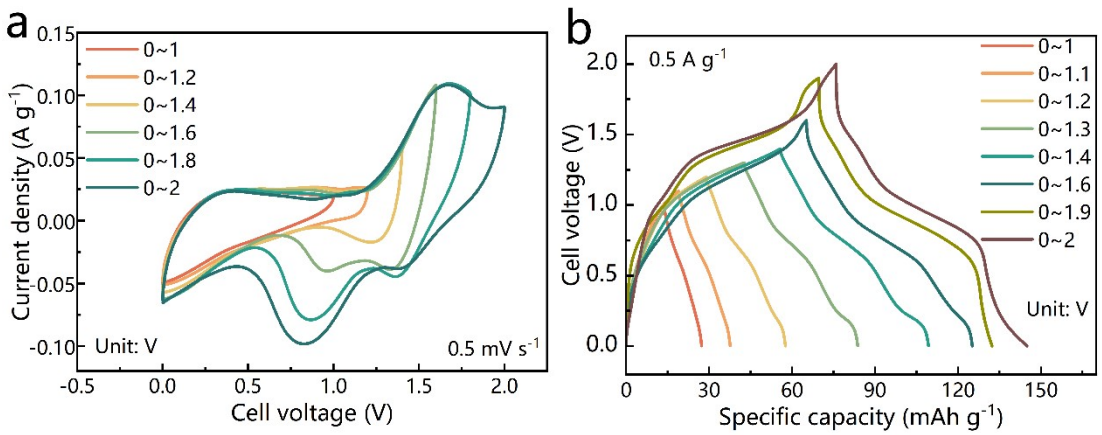


**Figure S16.** (a) CV curves of CuHCF//MVO AAIBs under different voltage windows at a scan rate of 0.5 mV $s^{-1}$, (d) GCD curves under different voltage windows at a current density of 0.5 A $g^{-1}$.